

Flexible Quasi-2D Perovskite/IGZO Phototransistors for Ultrasensitive and Broadband Photodetection

Shali Wei, Fang Wang, Xuming Zou,* Liming Wang, Chang Liu, Xingqiang Liu, Weida Hu, Zhiyong Fan, Johnny C. Ho,* and Lei Liao*

Organic–inorganic hybrid perovskites (PVKs) have recently emerged as attractive materials for photodetectors. However, the poor stability and low electrical conductivity still restrict their practical utilization. Owing to the quantum-well feature of two-dimensional (2D) Ruddlesden–Popper PVKs (2D PVKs), a promising quasi-2D PVK/indium gallium zinc oxide (IGZO) heterostructure phototransistor can be designed. By using a simple ligand-exchange spin-coating method, quasi-2D PVK fabricated on flexible substrates exhibits a desirable type-II energy band alignment, which facilitates effective spatial separation of photoexcited carriers. The device exhibits excellent photoresponsivity values of $>10^5 \text{ A W}^{-1}$ at 457 nm, and broadband photoresponse (457–1064 nm). By operating the device in the depletion regime, the specific detectivity is found to be 5.1×10^{16} Jones, which is the record high value among all PVK-based photodetectors reported to date. Due to the resistive hopping barrier in the quasi-2D PVK, the device can also work as an optoelectronic memory for near-infrared information storage. More importantly, the easy manufacturing process is highly beneficial, enabling large-scale and uniform quasi-2D PVK/IGZO hybrid films for detector arrays with outstanding ambient and operation stabilities. All these findings demonstrate the device architecture here provides a rational avenue to the design of next-generation flexible photodetectors with unprecedented sensitivity.

In the past decade, high-performance, low-cost, and robust photodetectors have become one of the key components for a wide range of commercial systems, including environment and security monitoring,^[1] wearable electronics,^[2] free-space communications,^[3] and biomedical diagnostics,^[4] etc. As inspired by these applications, various emerging materials, such as quantum dots,^[5] carbon nanotubes,^[6] graphene,^[7] and transition-metal dichalcogenides,^[8] are extensively explored for the efficient photodetection. In particular, organic–inorganic hybrid perovskites (OHPs) are lately considered as the superior light-harvesting materials for photodetectors owing to their unique advantages of high optical absorption coefficient, long exciton diffusion length, and low binding energy of exciton.^[9–11] Although these OHP materials can be easily prepared by cost-effective solution-based processes to meet the ever-increasing consumer demands for large-area and flexible optoelectronics, their photodetectors usually

exhibit the relatively low responsivity because of the limited carrier mobility as well as the absence of photoconductive gain (G) mechanism that can induce multiple charge carriers by one incident photon.


In order to tackle these insufficient device performances, hybrid phototransistors by simply integrating perovskites (PVKs) with different 2D materials (e.g., graphene,^[12] black phosphorus,^[13,14] MoS₂,^[15] and WSe₂^[16]) have been proposed and demonstrated. By using these hybrid heterostructures, upon illumination, the photoexcited charge carriers can be spatially separated at the hetero-interface in order to prolong their carrier lifetimes, which subsequently improves the photoconductive gain of the system. However, there are still significant concerns regarding the high fabrication cost and low production yield of 2D materials for the realization of such photodetectors. At the same time, due to the low formation energy, PVK photodetectors are generally susceptible to degradation upon air and moisture exposure. In this case, tremendous efforts have then been invested to explore effective approaches to enhance the ambient-stability of these devices.^[17,18] Among many latest advances, recent breakthroughs in achieving the 2D Ruddlesden–Popper phase of PVKs with the chemical formula of (RNH₃)₂(A)_{n-1}M_nX_{3n+1}, where RNH₃ is a large size or long-chain organic cation, A is a regular cation, M is a divalent

Dr. S. L. Wei, Prof. X. M. Zou, Dr. L. M. Wang, Dr. C. Liu,
Prof. X. Q. Liu, Prof. L. Liao
Key Laboratory for Micro/Nano Optoelectronic Devices of Ministry
of Education & Hunan Provincial Key Laboratory of Low-Dimensional
Structural Physics and Devices
School of Physics and Electronics
Hunan University
Changsha 410082, China
E-mail: zouxuming@hnu.edu.cn; liaolei@whu.edu.cn

Dr. F. Wang, Pro. W. D. Hu
State Key Laboratory of Infrared Physics
Shanghai Institute of Technical Physics
Chinese Academy of Sciences
Shanghai 200000, China

Prof. Z. Y. Fan
Department of Electronic and Computer Engineering
Hong Kong University of Science and Technology
Hong Kong SAR 999077, China

Prof. J. C. Ho
Department of Materials Science and Engineering
City University of Hong Kong
Tat Chee Avenue, Kowloon, Hong Kong SAR 999077, China
E-mail: johnnyho@cityu.edu.hk

 The ORCID identification number(s) for the author(s) of this article can be found under <https://doi.org/10.1002/adma.201907527>.

DOI: 10.1002/adma.201907527

metal cation, and X is a halide, are promising.^[19–22] These 2D PVKs can still be solution-processed and uniquely come with the quantum well structure formed by lead halide layers separated by hydrophobic organic cation spacer layers. Importantly, they have been illustrated with the exceptional robustness when they are configured into optoelectronic devices due to their excellent intrinsic chemical- and photostability.

In this article, we demonstrate a hybrid and cost-effective quasi-2D perovskite/indium gallium zinc oxide (quasi-2D PVK/IGZO) heterostructure phototransistor fabricated on a poly(ethylene terephthalate) (PET) substrate, in which this flexible device utilizes the ordered quantum well features of quasi-2D PVKs to obtain the ultrasensitive and highly stable photodetection. To be specific, a simple but robust ligand exchange method is employed to achieve the desired type-II energy band alignment of this device in the direction perpendicular to the substrate, ensuring the efficient spatial separation of photoexcited carriers. Meanwhile, the top IGZO film can function as a capping layer to prevent the underneath PVK from atmosphere exposure such that a superior stability is resulted in these PVK photodetectors. In this regard, this heterostructure phototransistor exhibits the ultrahigh specific detectivity (5.1×10^{16} Jones), broadband photoresponse (457–1064 nm), and unique photo-induced memory characteristics. All these results clearly indicate that the hybrid systems based on 2D PVKs are promising architecture to achieve high-performance and flexible photodetectors for practical applications.

The mechanically flexible quasi-2D PVK/IGZO phototransistor configured with the bottom-gate structure is schematically illustrated in Figure 1a. In details, the device channel, consisting of the bottom PVK light absorption layer and the upper IGZO carrier transport layer, is placed on top of the

Al_2O_3 dielectric layer. In this work, the 2D PVK is chosen to have the chemical formula of $(\text{PEA})_2(\text{MA})_{n-1}\text{Pb}_n\text{I}_{3n+1}$, where PEA^+ refers to $\text{C}_8\text{H}_9\text{NH}_3^+$, MA^+ represents CH_3NH_3^+ , and n defines the lead iodide octahedral layers between two PEA^+ organic spacers. Generally, phototransistors utilize the photo-gating effect to achieve a high gain (G) according to the following equation^[23]

$$G = \frac{\tau_{\text{lifetime}}}{\tau_{\text{transit}}} \quad (1)$$

where τ_{transit} denotes the transit time of carriers transporting within the channel and τ_{lifetime} denotes the lifetime of trapped photocarriers. It is apparent that one can enhance the ratio of $\tau_{\text{lifetime}}/\tau_{\text{transit}}$ in order to obtain the photoconductive gain. Since the τ_{transit} value is inversely proportional to the carrier mobility of channel material, integrating the IGZO here with the much higher carrier mobility than the one of PVK would be beneficial for reaching a high G in our devices (Figure S1, Supporting Information). In addition, increasing the τ_{lifetime} value would give the sufficient spatial separation of photoexcited electron-hole pairs to reduce recombination. As a result, a graded distribution of quasi-2D PVK quantum wells with type-II band alignment is highly favorable for high-gain phototransistors.

Impressively, when the 2D PVK film is prepared by conventional spin-coating, the inorganic layers composed by metal halides tend to extend parallel to the substrate plane, resulting in a unique cascaded structure of organic–inorganic alternating layers.^[24,25] In other words, this 2D PVK film can be considered naturally as a multiple quantum well structure, where the insulating organic layers serve as the “barrier” and the semi-conducting inorganic layers work as the “well.”^[24] In this case,

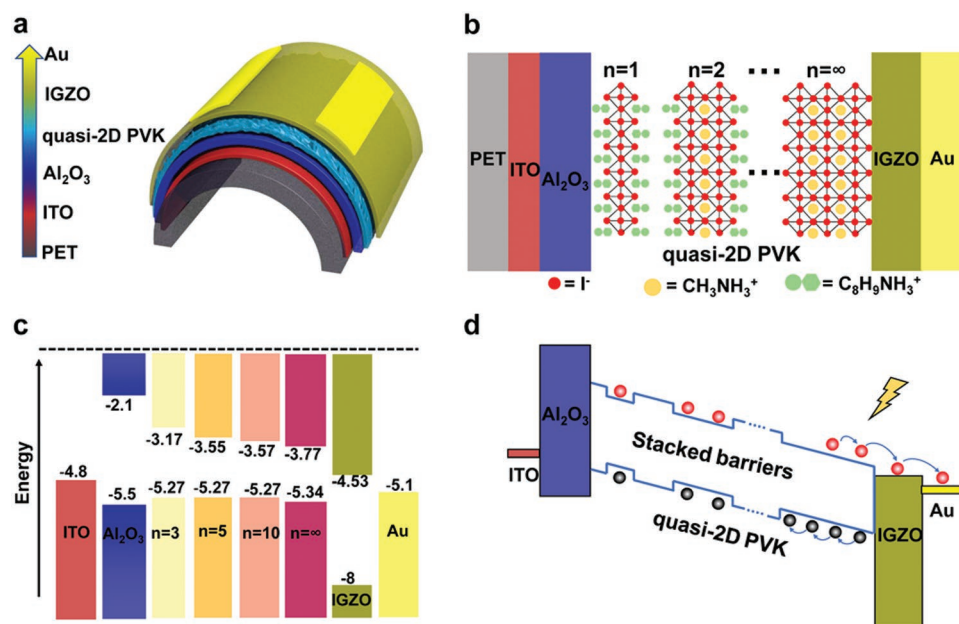


Figure 1. Operational mechanism of the quasi-2D PVK/IGZO heterostructure phototransistor. a) Schematic illustration of the quasi-2D PVK/IGZO phototransistor. b) The cross-section schematic of the device with different n values. Here, the 3D PVK structure is equivalent to $n = \infty$. c) Energy level alignment of the quasi-2D PVK/IGZO phototransistor, illustrating a slope existed in the energy band for the efficient photoexcited carrier separation. d) Schematic of the photoexcited charge transfer process in an ordered type-II energy band alignment. The photoexcited electrons would transfer from PVK into IGZO, while the hopping barrier in quasi-2D PVK quantum wells can hinder the photoexcited carrier recombination.

these quasi-2D PVKs with increasing n values would stack in a direction perpendicular to the substrate, offering the desirable band structure with type-II energy band bending (Figure 1b). This ordered distribution of 2D PVKs then results in a directed electron flow from low-dimension to high-dimension PVKs with the hole carriers flowing in an opposite manner. Simultaneously, simply by tuning the n values, the band structure of 2D PVKs would also change accordingly (Figure 1c).^[26] The conduction band minimum (CBM) is expected to increase with n , which allows the photoexcited electrons to be transferred efficiently from PVK into IGZO (Figure 1d). Meanwhile, the valence band maximum of all 2D PVKs is lower than that of IGZO, enabling the holes to move toward the Al_2O_3 /PVK interface. Furthermore, the hopping barriers are arranged in an orthogonal orientation that hinders the photoexcited carrier recombination and thus improves the photosensitivity greatly.

Regarding the device fabrication, the process flow of these flexible quasi-2D PVK/IGZO heterostructure phototransistor is illustrated in Figure 2a with the details described in the Experimental Section. Briefly, a 50 nm thick indium tin oxide (ITO) bottom-gate electrode was first deposited onto the PET substrate by magnetron sputtering. Then, a 100 nm thick Al_2O_3 dielectric layer was grown using atomic layer deposition (ALD), followed by the spin coating of quasi-2D PVK. Subsequently, an IGZO film was deposited with low-temperature magnetron sputtering to cover the PVK entirely. Here, although the finished quasi-2D/IGZO film exhibits a slightly increased root-mean-squared (RMS) surface roughness caused by the

low-temperature magnetron sputtering, X-ray diffraction (XRD) measurements indicate that there is not any noticeable lattice damage induced to the PVK film (Figure S2, Supporting Information). Finally, Cr/Au (15/50 nm) contact electrodes were patterned using thermal evaporation. The length (L_{ch}) and width (W_{ch}) of the IGZO channel are fixed to be 80 and 80 μm , respectively. It is worth noting that we obtained the desired quasi-2D PVK film through a two-step ligand exchange method (Figure 2a). At the first step, 30 μL of 2D PVK precursor solution, $\text{PEA}_2(\text{MA})_2\text{Pb}_3\text{I}_{10}$ ($n = 3$), preheated at 100 $^\circ\text{C}$ was spin-coated onto the substrate at 4000 rpm for 1 min. During this process, 5 μL of 3D PVK precursor solution, MAPbI_3 ($n = \infty$), preheated at 100 $^\circ\text{C}$ was dripped onto the substrate. Under the thermal energy action, the 3D PVK component is expected to diffuse into the 2D $\text{PEA}_2(\text{MA})_2\text{Pb}_3\text{I}_{10}$ PVK to constitute a vertical gradient of n values, achieving the above-mentioned type-II band alignment. The optical absorption spectrum of the obtained quasi-2D PVK film is shown in Figure S3 (Supporting Information). The distinctive bleach peaks indicate that the spin-coated quasi-2D PVK thin film comprises multiple phases with varying n values.

To shed light onto the phase distribution of this quasi-2D PVK film, photoluminescence (PL) spectra measurements are performed with two different incident light directions (Figure 2c). The 457 nm laser beam is either impinged through the PVK side (i.e., front excitation) or through the glass side (i.e., back excitation). The dominant PL spectra of three different PVK films (i.e., 2D $\text{PEA}_2(\text{MA})_2\text{Pb}_3\text{I}_{10}$, quasi-2D PVK, and

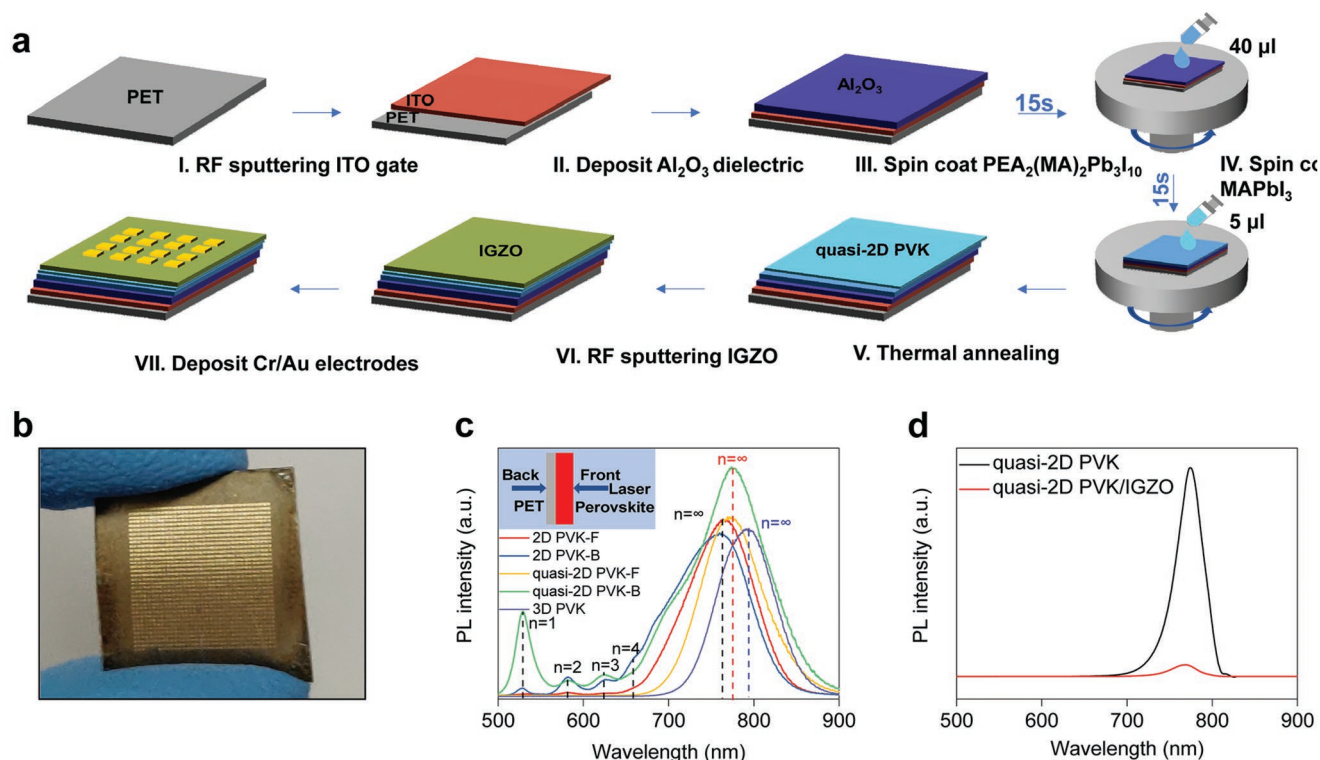


Figure 2. The preparation process and characterization of the 2D PVK/IGZO heterostructure phototransistor. a) The fabrication process of a flexible quasi-2D PVK/IGZO heterostructure phototransistor on a transparent PET substrate. b) Photograph of a typical flexible quasi-2D PVK/IGZO phototransistor under a bending state. c) The semilog scale curves of PL spectra of the 2D PVK, quasi-2D PVK, and 3D PVK illuminated from the back and front sides of the films; excitation at 457 nm. d) PL spectra of the quasi-2D PVK and quasi-2D PVK/IGZO films with a linear scale.

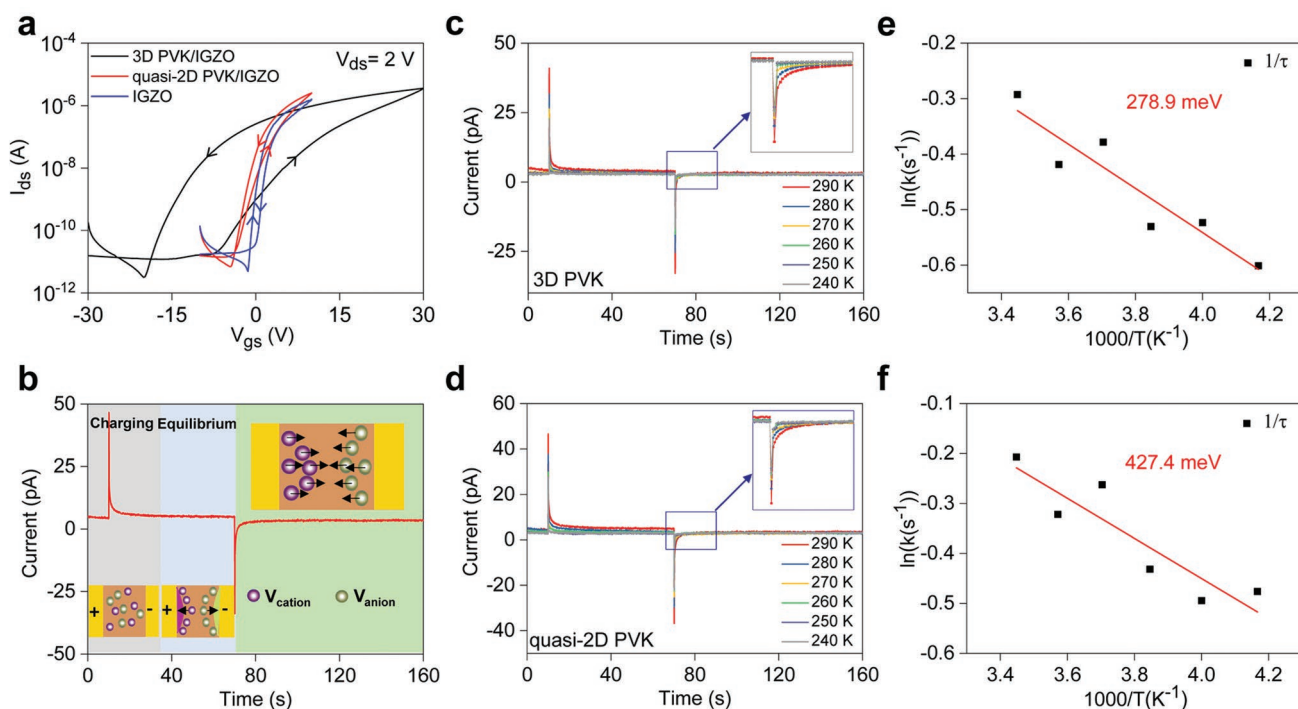


Figure 3. Measured ionic migration in 3D PVK and quasi-2D PVK films. a) Transfer characteristics of pristine IGZO, quasi-2D PVK/IGZO, and 3D PVK/IGZO phototransistors, respectively. b) The schematic illustration of a representative charging–discharging process for PVK device measured at 290 K. c) The temporal response curves under an external bias of 0.1 V for the quasi-2D PVK film device in the dark. d) The temporal response curves under an external bias of 0.1 V for the quasi-2D PVK film device in the dark. e) Arrhenius plot of the ion decay rate $1/\tau$ extracted from (c). The solid line presents the corresponding linear fitting result. f) Arrhenius plot of the ion decay rate $1/\tau$ extracted from (d). The solid line presents the corresponding linear fitting result.

3D MAPbI₃) are corresponded to the radiative recombination of the $n \approx \infty$ phase. In comparison with the 2D PVK, a redshift of the dominant peaks in quasi-2D and 3D PVKs are witnessed (765, 775, and 794 nm for 2D, quasi-2D, and 3D PVK, respectively), which implies an increase of the n values. This increased dimensionality results in a reduced bandgap due to the weaker dielectric confinement, indicating that different phase distribution is indeed achieved in the quasi-2D PVK. Moreover, for the 2D PVK of PEA₂(MA)₂Pb₃I₁₀, additional PL peaks arising from the PVK phases of $n = 1, 2, 3,$ and 4 are observed under both front and back excitation. On the contrary, the quasi-2D PVK exhibits a complete elimination of these minor emission peaks under front excitation. In view of the shallow penetration depth of 457 nm laser, these observations suggest that the phases with small n values are mainly located near the bottom surface while the ones with large n values are positioned toward the upper surface of the quasi-2D PVK film. This particular ordered phase distribution is anticipated to promote the directional photocarrier transport within the PVK film, in which this speculation is later confirmed by the PL measurement of quasi-2D PVK and quasi-2D PVK/IGZO heterostructure (Figure 2d). In contrast with the PVK-only film, a remarkable PL quenching of exceeding 95% is observed in the quasi-2D PVK/IGZO heterostructure under the same experimental condition, which serves as a direct evidence for the efficient separation of photoexcited carriers at the quasi-2D PVK/IGZO interface.

At present, the hysteresis issue of PVK devices still attracts the extensive attention because of its negative influence of the

scanning direction on the current–voltage curves of devices, which prevents the accurate evaluation of device performance and at the same time induces the premature device failure.^[27–29] Figure 3a demonstrates the typical transfer curves of IGZO, quasi-2D PVK/IGZO, and 3D PVK/IGZO PVK phototransistors, respectively. The scanning direction of gate bias is first manipulated from negative to positive voltages, and then back to negative voltages. For the IGZO device, the hysteresis loop is observed along the clockwise direction that can be attributed to the trapping of electrons from gate-induced high-conduction channels into immobile localized states. Accordingly, the device threshold voltage would shift toward the positive direction. On the other hand, by inserting a PVK layer between the IGZO and Al₂O₃ dielectric, the hysteresis loop turns into the anticlockwise direction. Apparently, this anticlockwise hysteresis cannot be explained by the trapping of negative charges into localized states. Previous studies have demonstrated the electric field-induced ion migration in perovskites.^[28,30,31] When PVKs are directly interfaced with the IGZO layer, there would be additional electric field caused by the directionally mobile ion under gate bias to induce additional charges in the IGZO channel, leading to the enhanced channel current with the anticlockwise hysteresis. If the electric field-driven ion migration is suppressed, then we can employ a larger gate bias to modulate the channel conductivity. In this case, the hysteresis window is found to be 1.8 V for IGZO, 2.1 V for quasi-2D PVK/IGZO, and 13.5 V for 3D PVK/IGZO devices, respectively. The smaller hysteresis observed for the quasi-2D PVK device implies a weakened ion migration there.

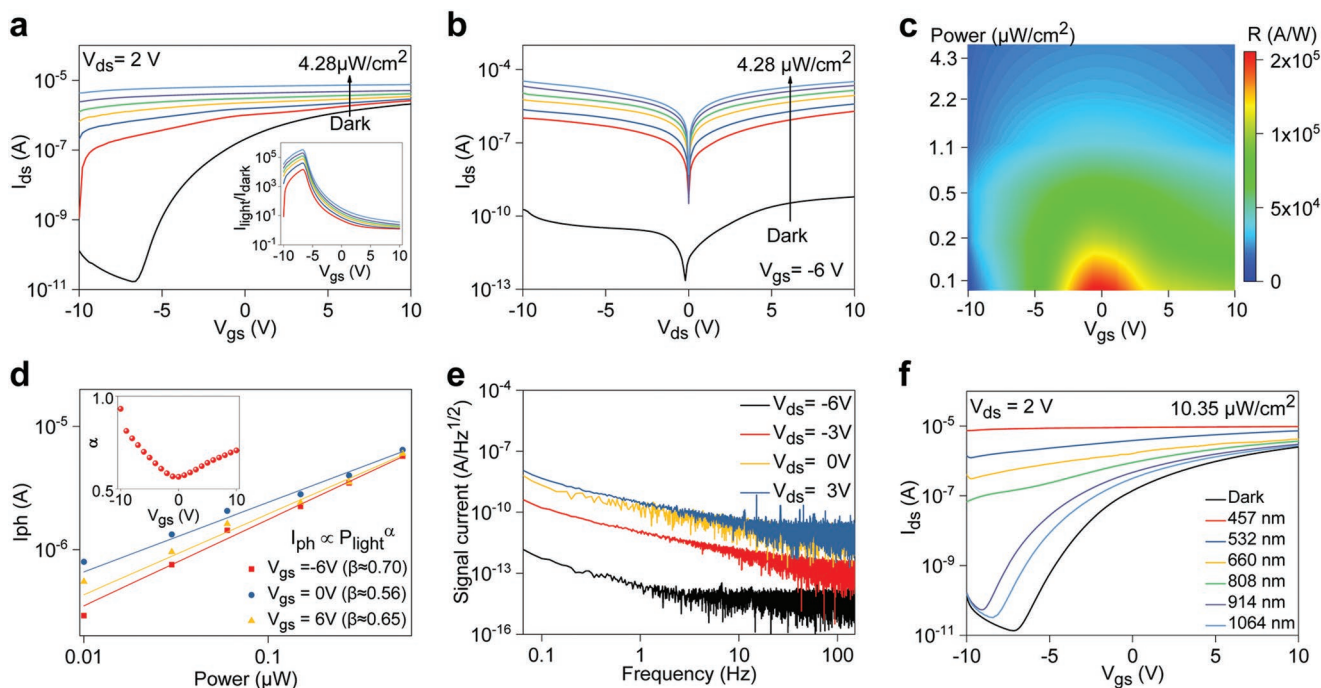


Figure 4. Optoelectronic characteristics of the 2D PVK/IGZO heterostructure phototransistor. a) Transfer characteristic curves under different P_{light} values at $V_{\text{ds}} = 2$ V. The inset shows the the light-to-dark current ratio under different P_{light} values. b) Output characteristic curves under different P_{light} values at $V_{\text{gs}} = -7$ V. c) V_{gs} and P_{light} dependent responsivity extracted from transfer characteristic curves in (a). d) The I_{ph} values plotted as a function of incident power. The inset shows the extracted exponent α for different V_{gs} values. e) Noise analysis of the IGZO-PVK phototransistor extracted from the Fourier transform of the dark current. f) Transfer characteristic curves under different wavelength lasers.

Furthermore, in OHPs, it is well known that the ion diffusion barrier depends primarily on the rotation and orientation of nearby organic molecules toward the electric field direction. Here, the weakened structural relaxation in quasi-2D PVK by long-chain cations is expected to suppress the ion migration greatly. In order to quantitatively understand the ion migration process, we utilize the method demonstrated by Duan et al. to perform electrical measurements on vertically stack Au/PVK/Au devices.^[32] Figure 3b illustrates the schematic diagram of the activation energy extraction for ionic migration in PVK. After exerting an external bias to the device, an obvious current spike is observed due to the much faster drift speed of electrons/holes than ions. At the same time, anion and cation vacancies (e.g., V_{I} , V_{Pb} , and so on) also get drifted along the external electric field direction and gradually accumulated close to Au electrodes, resulting in an internal electric field. This developed field would then weaken the external electric field and reduces the electron/hole current until a stable equilibrium achieved. Once the external bias is removed, the accumulated ions would move again to restore the initial distribution because of the concentration gradient, leading to a reverse decaying current. According to the decay rate, we can extract the ion transport activation energy (see the Experimental Section for details). The activation energy is estimated to be 278.9 meV for 3D PVK MAPbI₃ (Figure 3c–e), slightly different from that of previous report.^[29] In contrast, the quasi-2D PVK exhibits a much higher activation energy of 427.4 meV (Figure 3d–f), indicating the ion migration in our quasi-2D PVK indeed more difficult and get suppressed.

Based on the quasi-2D PVK quantum well structure with desirable type-II energy band bending as well as the suppressed

ionic migration, it is worth to investigate the performance limits of these quasi-2D PVK quantum well/IGZO heterostructure phototransistors. Figure 4a shows the device transfer curves under different incident power at $V_{\text{ds}} = 2$ V with V_{gs} sweeping from -10 to 10 V. The corresponding gate leakage curves are given in Figure S4 (Supporting Information). In specific, even at an ultralow power density of $0.08 \mu\text{W cm}^{-2}$, there is an obvious threshold voltage shift of 3.3 V observed toward the negative direction. In view of the n -type characteristics of IGZO, this shift is typically referred to the trapping of photoexcited holes, which is capable to modulate the capacitance of the IGZO channel to induce the pronounced photogating effect. Figure 4a inset displays the light-to-dark current ratio ($I_{\text{light}}/I_{\text{dark}}$), which is a typical parameter employed to evaluate the degree of obtrusive noise. It is clear that the $I_{\text{light}}/I_{\text{dark}}$ value gets increased with the increasing incident light intensity (P_{light}), which exhibits a maximum value of 3.3×10^5 at $P_{\text{light}} = 4.28 \mu\text{W cm}^{-2}$. Under dark, the hybrid phototransistor is operated in an off-state for $V_{\text{gs}} = -6$ V (Figure 4b). With light illumination, photoexcited electrons are then injected into the IGZO channel, whereas the device output current is amplified significantly by the photogating effect.

Apart from that, we further characterize the photoresponsivity (R) as a function of gate voltage varying from -10 to 10 V under different incident light powers (Figure 4c). In explicit, the R value is defined as the following^[33]

$$R = \frac{I_{\text{light}} - I_{\text{dark}}}{P_{\text{light}}S} = \frac{I_{\text{ph}}}{P_{\text{light}}S} \quad (2)$$

where I_{ph} denotes the photocurrent, and S represents the active area of photodetector. It is expected that the responsivity gradually decreases with the increasing light intensity, which is attributable to the higher recombination rate of photoexcited carriers in the PVK layer. When gate voltage is ≈ 0 V, R reaches its maximum value of 3.1×10^5 A W⁻¹. This value is three orders of magnitude higher than the one previously reported for graphene/3D PVK hybrid phototransistor, which evidently demonstrates the superior performance achieved in our devices. It is also noted that the responsivity gets monotonically decreased as gate voltage decreases to -10 V or increases to 10 V. This V_{gs} dependent responsivity can be explained with the effective modulation of Schottky barrier height (SBH) and carrier density at the Cr/IGZO interface and in the IGZO channel, respectively (Figure S5, Supporting Information). Under light illumination, excitons or electron–hole pairs are generated efficiently in the quasi-2D PVK layer and then swept at the quasi-2D PVK/IGZO interface driving by the built-in electric field established there. Subsequently, the photoexcited electrons would transfer into the IGZO layer and circulate under the applied source–drain bias, whereas the photoexcited holes are trapped in the quasi-2D PVK layer, efficiently modulating the conduction of IGZO channel through capacitive coupling. At $V_{\text{gs}} = 0$ V, the Fermi level (E_{F}) of IGZO is close to the CBM due to n-type doping induced by the quasi-2D PVK. The small SBH between Cr electrode and IGZO enables the highly efficient photocurrent generation, including both thermionic and tunneling current, to yield a strong photogating effect. When turning the device into an off-state by decreasing the V_{gs} value, the E_{F} of IGZO would shift down near the midgap and induces a large SBH value. This hinders the photoexcited electron drifting to the external circuit to give a low photoresponsivity. In contrast, once the positive gate voltage is applied, the E_{F} can move into the conduction band and the IGZO device would operate in the saturation state. This way, majority of the states with the conduction band are occupied. Thus, a large amount of photoexcited carriers would recombine in the PVK quickly, leading to a suppressed photogating effect. To confirm the above-mentioned mechanism, we plot the photocurrent as a function of P_{light} with different V_{gs} values (Figure 4d). The obtained curves can be fitted well with an equation of $I_{\text{ph}} \propto P_{\text{light}}^{\alpha}$, where α is a constant. In general, $\alpha = 1$ represents a pure photoconductive effect, while $\alpha < 1$ indicates the existence of a photogating effect.^[34] All extracted α values are determined to be less than 1, which suggests the existence of photogating effect. It is also observed that the variation of α values is perfectly consistent with the device photoresponsivity, reaching its minimum value of 0.56 at $V_{\text{gs}} = 0$ V. This consistency reveals that the photogating effect is the dominating mechanism responsible for the enhanced photocurrent in our devices.

Next, we assess the specific detectivity (D^*) of our devices, which is one of the figure-of-merits for a photodetector in detecting weak optical signals. The D^* value can be evaluated with the equation^[35,36]

$$D^* = \frac{(\text{SB})^{1/2}}{\text{NEP}} \quad (3)$$

$$\text{NEP} = \frac{i_n^{2-1/2}}{R} \quad (4)$$

where B denotes the bandwidth, NEP refers to the the noise equivalent power, and $i_n^{2-1/2}$ represents the RMS value of the noise current. Figure 4e exhibits the $i_n^{2-1/2}$ value measured at different gate voltages in order to determine the detectivity. At $V_{\text{gs}} = 3$ V, the device displays a clear $1/f$ -noise component, while a flat line of spectral noise density starts to emerge at $V_{\text{gs}} = -6$ V due to the noise floor of the measuring instrument. The noise level per unit bandwidth (1 Hz) of the phototransistor is measured to be 1.9×10^{-14} , 1.1×10^{-11} , 1.0×10^{-10} , and 2.4×10^{-10} pA/Hz^{1/2} under the operational gate voltages of -6 , -3 , 0 , and 3 V, respectively. Despite the highest responsivity value at $V_{\text{gs}} = 0$ V, the detectivity exhibits its lowest value due to the high noise at such high dark current. The D^* value would then get improved for the more negative gate voltage, reaching its maximum value of 5.1×10^{16} Jones at $V_{\text{gs}} = -6$ V (Figure S6, Supporting Information), where this D^* value is already four orders of magnitude higher than the one of traditional Si photodetectors ($\approx 4 \times 10^{12}$ Jones).^[37] Such an ultrahigh detectivity can provide a quantitative evidence that the device configuration presented here is extremely suitable for the detection of small optical input signals. In addition, to the best of our knowledge, this detectivity of 10^{16} Jones constitutes the record high value among all PVK-based photodetectors reported in the literature, since our device design and performance are not limited by the obstacles in achieving both high responsivity and low dark current at the same time.

Although the above measurements are all focused on the photoresponse to 457 nm light, it is also important to evaluate the spectral response of these photodetectors (Figure 4f). Notably, the laser power intensity is fixed at $10.35 \mu\text{W cm}^{-2}$ for all measurements here. It is obvious that the device gives a high photoresponse to 457 nm light as well as to the light of longer wavelengths. For the wavelengths beyond 760 nm, the optical absorption of the PVK becomes relatively low, but the responsivity of the device can maintain as high as 526 A W^{-1} at 1064 nm (Figure S7, Supporting Information). This impressive photoresponse in the near-infrared regime beyond the absorption edge of PVK can be attributed to the efficient excitation of carriers from the valence band to the traps states within the PVK bandgap, being similar to the extrinsic photoconductors based on conventional semiconductors.^[38]

Besides, memory devices are another important device components in the electronic information industry.^[39,40] For instance, the optoelectronic memory devices, which can convert electromagnetic radiation into storable electric signals, are extremely attractive for optical recording.^[41–43] Interestingly, apart from photodetection, our photogate quasi-2D PVK/IGZO heterostructure can also be employed for the photo-induced memory applications (Figure 5a). In this case, in view of the dominant role of near-infrared light in optical communication, night vision, and spectroscopy, we focus on characterizing the near-infrared storage of our devices. When the laser ($15.6 \mu\text{W cm}^{-2}$, 1064 nm) is illuminated onto the device, the I_{ds} rapidly increases to a maximum value with a writing time of 6 s due to the process of programmed light signal. Then, it quickly drops to an optimum value and reaches its photocurrent stability (Figure 5a inset). Such a sharp current rise can be attributed to the sudden increase of photoexcited electrons in the IGZO channel when first exposing to light. The subsequent

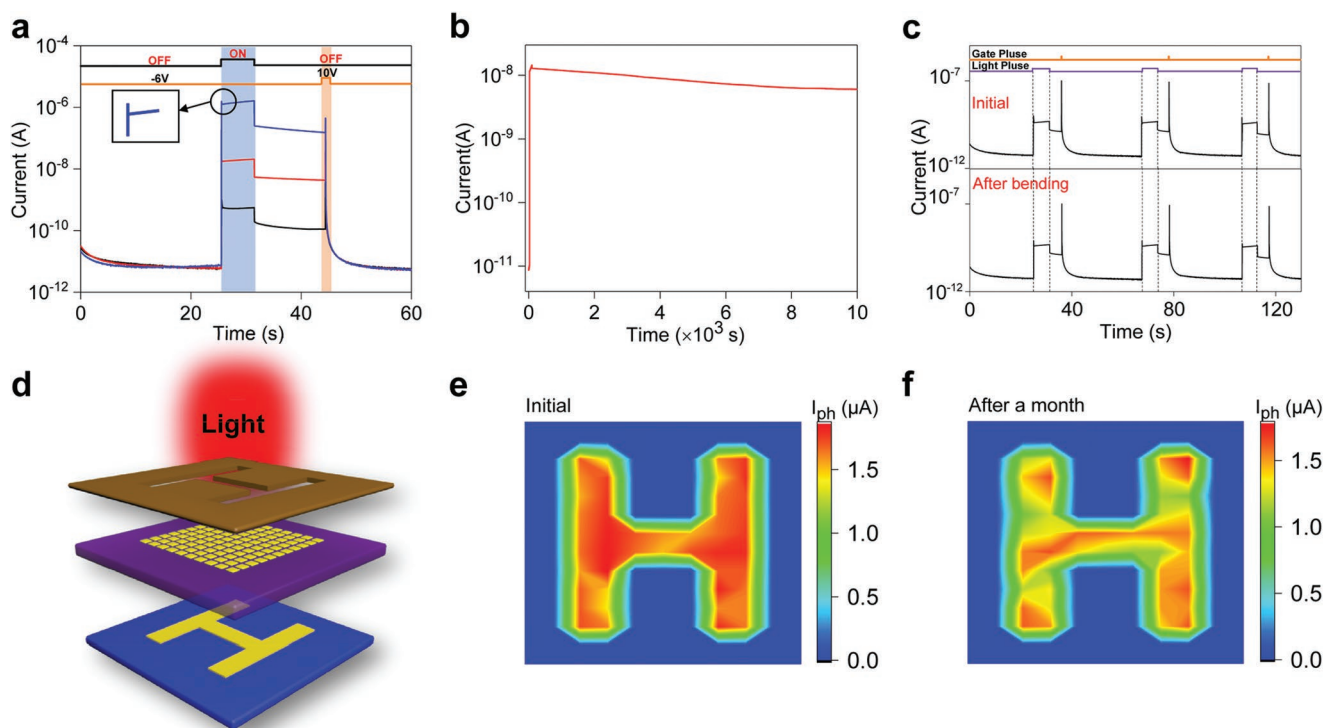


Figure 5. The storage, flexibility, and stability characteristics of the 2D PVK/IGZO heterostructure phototransistor. a) Writing and erasing processes of the device under infrared laser pulse (1064 nm) and V_{gs} pulse, respectively. The power density of the infrared pulse is 15.6, 24.6, and 2672.2 $\mu\text{W cm}^{-2}$ with a duration of 5 s. The inset indicates an instant increase of source–drain current when the gate voltage pulse is applied. The shade of blue represents the laser pulse. b) The charge storage stability of the photo-induced memory device. c) Program, storage, and erase of the infrared signal before and after 300 bending cycles. d) Schematic illustration of a flexible 2D PVK/IGZO photodetector array for multipoint light distribution detection. e) Photocurrent mapping of the photodetector arrays with the H-shaped mask. f) Photocurrent mapping of the photodetector arrays with the H-shaped mask upon atmosphere exposure for 1 month.

current decrease and its current stabilization are probably due to the traps existed in the slightly surface-roughened quasi-2D PVK and IGZO films, where these traps can capture parts of photoexcited carriers quickly. When the laser is turned off, the enhanced I_{ds} stays on a high level and shows a long relaxation time, leading to a metastable state with high conductivity. This metastable state can be ascribed to the hopping barrier established in quasi-2D PVK, which induces the slow release of photoexcited holes in the PVK layer as well as the suppressed recombination of photoexcited carriers. Finally, the applied gate bias is varied from -6 to 10 V for 0.03 s in order to erase the stored optical signal such that the device can return to its non-conducting initial state. This way, the entire process constitutes a complete dynamic working cycle of an optoelectronic memory device, including programming, storing, and erasing optical signals. The schematic diagram of near-infrared memory operation and V_{gs} pulse cancellation are shown in Figure S8 (Supporting Information). We also achieve three distinct resistance states programmed by the light intensity modulation. Figure 5b presents the retention time of photo-induced persistent photocurrent under a long measurement duration of exceeding 10^4 s. It is found that the current decays extremely slowly during the entire measurement range, which demonstrates the feasibility of nonvolatile optical signal storage for these quasi-2D PVK/IGZO device. Figure 5c shows the three complete dynamic working cycles before and after repetitive bending for 300 times.

The device performance gives an unnoticeable change upon the bending test, indicating a promising future of these devices for mechanically flexible applications.

Finally, we as well construct large-scale device arrays to evaluate their scalability for the applications of real-time light trajectories and multipoint light distribution systems. As shown in Figure 5d, the pixels generate the higher current values for the letter pattern area with light illumination, while the other pixels give the dark current with insignificant variations for the region blocked by the designed mask. As a result, a clear letter “H” can be identified in the mapping results, which indicates the excellent imaging performance of fabricated flexible photodetector arrays. In order to investigate their long-term stability, we test the device operation when they are freshly made (Figure 5e), stored for 1 week (Figure S9, Supporting Information) and 1 month (Figure 5f) in details for comparison. Remarkably, the photocurrent variation of less than 20% is obtained, indicating the excellent long-term stability of the photodetector arrays. X-ray diffraction measurement upon atmosphere exposure further indicates that the IGZO capping layer plays a key role in stabilizing the devices, which can prevent the direct contact between quasi-2D PVK and adventitious water moisture (Figure S10, Supporting Information). All these results evidently demonstrate the stable and efficient real-time light trajectory tracking and imaging of our devices.

In summary, we have demonstrated the large-scale flexible device arrays based on quasi-2D PVK/IGZO heterojunctions for efficient photodetection and imaging. By using the simple two-step ligand exchange spin-coating, the PVK film fabricated on flexible substrates are observed to have the desirable type-II energy band alignment. This ideal band bending facilitates the effective spatial separation of photoexcited carriers, which greatly enhances the photoconductive gain of obtained devices. Under illumination, the device exhibits the outstanding photoresponse properties, including a high responsivity of $3.1 \times 10^5 \text{ A W}^{-1}$ and a record high specific detectivity up to 5.1×10^{16} Jones. Furthermore, the device possesses the excellent electrical stability after hundreds of bending cycles as well as long-time storage in atmosphere. More importantly, the photocurrent can maintain its stability exceeding 10^4 s until it is erased by the positive V_{gs} pulse. This makes the device attractive for photo-induced memory applications. All these results clearly illustrate the great potential of quasi-2D PVK/IGZO phototransistors for next-generation flexible optoelectronic devices.

Experimental Section

Materials Synthesis and Device Fabrication: 3D PVK MAPbI_3 precursor solution was prepared by dissolving MAI and PbI_2 with a 1:1 molar ratio in N,N-dimethylformamide (N,N-DMF). 2D PVK precursor solution was prepared by dissolving PEAI, MAI, and PbI_2 with a 2:2:3 molar ratio in N,N-DMF. In both solutions, the molar concentration of Pb^{2+} was controlled to be 0.15 M.

The ITO gate electrodes (50 nm) was first deposited on a PET substrate using radio-frequency sputtering. Then, a 100 nm thick Al_2O_3 dielectric layer was deposited by ALD (precursor: trimethylaluminum and water; deposition temperature = 95 °C). Subsequently, 30 μL of preheated 2D $\text{PEA}_2(\text{MA})_2\text{Pb}_3\text{I}_{10}$ solution (100 °C) was spin-coated onto the substrate at 4000 rpm. After 15 s, 5 μL preheated MAPbI_3 precursor solution (100 °C) was dripped onto the spinning substrate. After another 45 s, the spinning process ended. The resulting film was subsequently annealed for 1 h at 100 °C for the better crystallization. Next, an IGZO film (around 60 nm) was deposited on the PET substrate using sputtering with a single target ($\text{In}_2\text{O}_3:\text{Ga}_2\text{O}_3:\text{ZnO} = 1:1:1$ atom%). The sputtering power was 15 W, while the vacuum was maintained at 0.6 Pa. Finally, quasi-2D PVK/IGZO heterostructure phototransistor arrays were achieved by the thermal evaporation of 50 nm Au as source/drain electrodes.

Materials Characterization and Electrical Measurements: The PL spectra of the films were recorded at room temperature using WITec alpha 300R. Electrical and optoelectronic properties were measured by an Agilent B1500A and B2912A semiconductor parameter analyzer. The low-temperature electrical measurements were performed with the Lake Shore TTPX probe station. The laser source was a laser with wavelengths of 457, 532, 660, 808, 914, and 1064 nm, respectively. XRD measurement was performed by X-ray diffraction spectrometer (XRD-6100, SHIMADZU) operating at room temperature. The surface morphologies of the PVK film were characterized by a scanning atomic force microscope using XE-7, Park Systems Corp.

Calculation of Ionic Migration: The dynamic of ion motion was fully reflected in the decay of the negative current. Therefore, the negative current decay curve using the biexponential function can be fitted

$$I(t) = I_0 + (I_e - I_1) \exp\left(-\frac{t - t_0}{\tau_e}\right) + (I_1 - I_0) \exp\left(-\frac{t - t_0 - \gamma}{\tau}\right) \quad (5)$$

where I_0 denotes the constant current of the Au/PVK/Au device under equilibrium conditions without external bias as shown in Figure 3c,d; I_1 represents the instant current as the external bias is removed at $t_0 + \gamma$;

τ denotes the time constant of ion diffusion and restoration; t_0 refers to the time right after the removal of applied external bias; τ_e and I_e relate to the RC delay of the equipment. By fitting the negative current decay curve, the τ value can be extracted. Because the decay rate $k = 1/\tau$ reflects the ionic transport dynamics, the activation energy of ion transport can be extracted by fitting the temperature-dependent decay rate, k , with Arrhenius equation

$$\ln(k) = C - \frac{E_a}{k_B T} \quad (6)$$

where C denotes a constant, E_a represents the activation energy, k_B refers to Boltzmann's constant, and T denotes the temperature.

Supporting Information

Supporting Information is available from the Wiley Online Library or from the author.

Acknowledgements

S.L.W. and F.W. contributed equally to this work. This work was financially supported by the National Key Research and Development Program of Ministry of Science and Technology (No. 2018YFB0406603), National Natural Science Foundation of China (Grant Nos. 61925403, 61851403, 61811540408, 51872084, and 61704051), the Strategic Priority Research Program of Chinese Academy of Sciences (Grant No. XDB30000000), as well as the Natural Science Foundation of Hunan Province (Nos. 2017RS3021 and 2017JJ3033).

Conflict of Interest

The authors declare no conflict of interest.

Keywords

broadband photodetection, IGZO, perovskites, phototransistors

Received: November 16, 2019

Revised: December 8, 2019

Published online:

- [1] U. Willer, M. Saraji, A. Khorsandi, P. Geiser, W. Schade, *Opt. Lasers Eng.* **2006**, *44*, 699.
- [2] J. Kim, I. Jeeran, S. Imani, T. N. Cho, A. Bandodkar, S. Cinti, P. P. Mercier, J. Wang, *ACS Sens.* **2016**, *1*, 1011.
- [3] R. Soref, *Nat. Photonics* **2010**, *4*, 495.
- [4] S. Choi, H. Lee, R. Ghaffari, T. Hyeon, D. H. Kim, *Adv. Mater.* **2016**, *28*, 4203.
- [5] Z. Sun, Z. Liu, J. Li, G. A. Tai, S. P. Lau, F. Yan, *Adv. Mater.* **2012**, *24*, 5878.
- [6] D. Jariwala, V. K. Sangwan, C. C. Wu, P. L. Prabhurashi, M. L. Geier, T. J. Marks, L. J. Lauhon, M. C. Hersam, *Proc. Natl. Acad. Sci. USA* **2013**, *110*, 18076.
- [7] S. Goossens, G. Navickaite, C. Monasterio, S. Gupta, J. J. Piqueras, R. Pérez, G. Burwell, I. Nikitskiy, T. Lasanta, T. Galán, E. Puma, A. Centeno, A. Pesquera, A. Zurutuza, G. Konstantatos, F. Koppens, *Nat. Photonics* **2017**, *11*, 366.
- [8] J. Y. Wu, Y. T. Chun, S. Li, T. Zhang, J. Wang, P. K. Shrestha, D. Chu, *Adv. Mater.* **2018**, *30*, 1705880.

- [9] S. F. Leung, K. T. Ho, P. K. Kung, V. K. S. Hsiao, H. N. Alshareef, Z. L. Wang, J. H. He, *Adv. Mater.* **2018**, *30*, 1704611.
- [10] J. Zhou, J. Huang, *Adv. Sci.* **2018**, *5*, 1700256.
- [11] F. P. García de Arquer, A. Armin, P. Meredith, E. H. Sargent, *Nat. Rev. Mater.* **2017**, *2*, 16100.
- [12] Y. Lee, J. Kwon, E. Hwang, C. H. Ra, W. J. Yoo, J. H. Ahn, J. H. Park, J. H. Cho, *Adv. Mater.* **2015**, *27*, 41.
- [13] L. Wang, X. Zou, J. Lin, J. Jiang, Y. Liu, X. Zhao, Y. F. Liu, J. C. Ho, L. Liao, *ACS Nano* **2019**, *13*, 4804.
- [14] X. Zou, Y. Li, G. Tang, P. You, F. Yan, *Small* **2019**, *15*, 1901004.
- [15] Y. Wang, R. Fullon, M. Acerce, C. E. Petoukhoff, J. Yang, C. Chen, S. Du, S. K. Lai, S. P. Lau, D. Voiry, D. O'Carroll, G. Gupta, A. D. Mohite, S. Zhang, H. Zhou, M. Chhowalla, *Adv. Mater.* **2017**, *29*, 1603995.
- [16] H. C. Cheng, G. Wang, D. Li, Q. He, A. Yin, Y. Liu, H. Wu, M. Ding, Y. Huang, X. Duan, *Nano Lett.* **2016**, *16*, 367.
- [17] G. Niu, X. Guo, L. Wang, *J. Mater. Chem. A* **2015**, *3*, 8970.
- [18] H. Tan, A. Jain, O. Voznyy, X. Lan, F. P. García de Arquer, J. Z. Fan, R. Q. Bermudez, M. Yuan, B. Zhang, Y. Zhao, F. Fan, P. Li, L. N. Quan, Y. Zhao, Z. H. Lu, Z. Yang, S. Hoogland, E. H. Sargent, *Science* **2017**, *355*, 722.
- [19] H. Tsai, W. Nie, J. C. Blancon, C. C. Stoumpos, R. Asadpour, B. Harutyunyan, A. J. Neukirch, R. Verduzco, J. J. Crochet, S. Tretiak, L. Pedesseau, J. Even, M. A. Alam, G. Gupta, J. Lou, P. M. Ajayan, M. J. Bedzyk, M. G. Kanatzidis, *Nature* **2016**, *536*, 312.
- [20] H. Cho, Y. H. Kim, C. Wolf, H. D. Lee, T. W. Lee, *Adv. Mater.* **2018**, *30*, 1704587.
- [21] Y. Liang, Q. Shang, Q. Wei, L. Zhao, Z. Liu, J. Shi, Y. Zhong, J. Chen, Y. Gao, M. Li, X. Liu, G. Xing, Q. Zhang, *Adv. Mater.* **2019**, *31*, 1903030.
- [22] J. Shi, Y. Gao, X. Gao, Y. Zhang, J. Zhang, X. Jing, M. Shao, *Adv. Mater.* **2019**, *31*, 1901673.
- [23] G. Konstantatos, M. Badioli, L. Gaudreau, J. Osmond, M. Bernechea, F. P. Garcia de Arquer, F. Gatti, F. H. Koppens, *Nat. Nanotechnol.* **2012**, *7*, 363.
- [24] H. Tsai, R. Asadpour, J. C. Blancon, C. C. Stoumpos, J. Even, P. M. Ajayan, M. G. Kanatzidis, M. A. Alam, A. D. Mohite, W. Nie, *Nat. Commun.* **2018**, *9*, 2130.
- [25] L. Pedesseau, D. Saporì, B. Traore, R. Robles, H. H. Fang, M. A. Loi, H. Tsai, W. Nie, J. C. Blancon, A. Neukirch, S. Tretiak, A. D. Mohite, C. Katan, J. Even, M. Kepenekian, *ACS Nano* **2016**, *10*, 9776.
- [26] M. Yuan, L. N. Quan, R. Comin, G. Walters, R. Sabatini, O. Voznyy, S. Hoogland, Y. Zhao, E. M. Beauregard, P. Kanjanaboos, Z. Lu, D. H. Kim, E. H. Sargent, *Nat. Nanotechnol.* **2016**, *11*, 872.
- [27] H. J. Snaith, A. Abate, J. M. Ball, G. E. Eperon, T. Leijtens, N. K. Noel, S. D. Stranks, J. T. Wang, K. Wojciechowski, W. Zhang, *J. Phys. Chem. Lett.* **2014**, *5*, 1511.
- [28] C. Eames, J. M. Frost, P. R. Barnes, B. C. O'Regan, A. Walsh, M. S. Islam, *Nat. Commun.* **2015**, *6*, 7497.
- [29] S. Meloni, T. Moehl, W. Tress, M. Franckevicius, M. Saliba, Y. H. Lee, P. Gao, M. K. Nazeeruddin, S. M. Zakeeruddin, U. Rothlisberger, M. Graetzel, *Nat. Commun.* **2016**, *7*, 10334.
- [30] Z. Xiao, Y. Yuan, Y. Shao, Q. Wang, Q. Dong, C. Bi, P. Sharma, A. Gruverman, J. Huang, *Nat. Mater.* **2015**, *14*, 193.
- [31] Y. Yuan, J. Huang, *Acc. Chem. Res.* **2016**, *49*, 286.
- [32] D. Li, H. Wu, H. C. Cheng, G. Wang, Y. Huang, X. Duan, *ACS Nano* **2016**, *10*, 6933.
- [33] F. H. Koppens, T. Mueller, P. Avouris, A. C. Ferrari, M. S. Vitiello, M. Polini, *Nat. Nanotechnol.* **2014**, *9*, 780.
- [34] C. Hu, D. Dong, X. Yang, K. Qiao, D. Yang, H. Deng, S. Yuan, J. Khan, Y. Lan, H. Song, J. Tang, *Adv. Funct. Mater.* **2017**, *27*, 1603605.
- [35] D. Shao, J. Gao, P. Chow, H. Sun, G. Xin, P. Sharma, J. Lian, N. A. Koratkar, S. Sawyer, *Nano Lett.* **2015**, *15*, 3787.
- [36] X. Liu, L. Gu, Q. Zhang, J. Wu, Y. Long, Z. Fan, *Nat. Commun.* **2014**, *5*, 4007.
- [37] E. Liu, M. Long, J. Zeng, W. Luo, Y. Wang, Y. Pan, W. Zhou, B. Wang, W. Hu, Z. Ni, Y. You, X. Zhang, S. Qin, Y. Shi, K. Watanabe, T. Taniguchi, H. Yuan, H. Y. Hwang, Y. Cui, F. Miao, D. Xing, *Adv. Funct. Mater.* **2016**, *26*, 1938.
- [38] S. W. Teitworth, R. M. Westervelt, *Phys. Rev. Lett.* **1984**, *53*, 2587.
- [39] M. H. Lankhorst, B. W. Ketelaars, R. A. Wolters, *Nat. Mater.* **2005**, *4*, 347.
- [40] H. S. Wong, S. Salahuddin, *Nat. Nanotechnol.* **2015**, *10*, 191.
- [41] A. Star, Y. Lu, K. Bradley, G. Gruner, *Nano Lett.* **2004**, *4*, 1587.
- [42] Q. Wang, Y. Wen, K. Cai, R. Cheng, L. Yin, Y. Zhang, J. Li, Z. Wang, F. Wang, F. Wang, T. A. Shifa, C. Jiang, H. Yang, J. He, *Sci. Adv.* **2018**, *4*, eaap7916.
- [43] J. Borghetti, V. Derycke, S. Lenfant, P. Chenevier, A. Filoramo, M. Goffman, D. Vuillaume, J. P. Bourgoin, *Adv. Mater.* **2006**, *18*, 2535.